THE JOURNAL OF PHYSICAL CHEMISTRY C

Article

pubs.acs.org/JPCC

Characterization of Primary Carrier Transport Properties of the Light-Harvesting Chalcopyrite Semiconductors $CuIn(S_{1-x}Se_x)_2$

Jessica J. Frick, Satya K. Kushwaha, Robert J. Cava,* and Andrew B. Bocarsly*

Department of Chemistry, Princeton University, Princeton, New Jersey 08544, United States

ABSTRACT: We report the carrier transport properties of $CuIn(S_{1-x}Se_x)_2$ ($0 \leq x \leq 1$), a promising chalcopyrite semiconductor series for solar water splitting. A low concentration Mg dopant is used to decrease the carrier resistivity through facilitating bulk *p*-type transport at ambient temperature. Temperature-dependent resistivity measurements reveal a four-order magnitude decrease in bulk electrical resistivity (from 10^3 to 10^{-1} Ohm cm) for 1% Mg-doped $CuIn(S_{1-x}Se_x)_2$ as x increases from 0 to 1. Hall effect measurements at room temperature reveal *p*-type majority carrier concentrations that vary from 10^{15} to 10^{18} cm^{-3} and mobilities of approximately 1−10 cm^2 V^{-1} s^{-1}. These results provide insights into the fundamental carrier transport properties of $CuIn(S_{1-x}Se_x)_2$ and will be of value in optimizing these materials further for photoelectrochemistry applications.

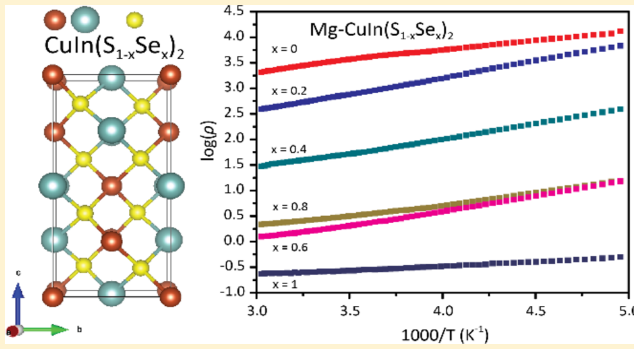

■ INTRODUCTION

To enhance optical to electrical conversion efficiencies in photoelectrochemical (PEC) measurements, work has been directed toward improving charge separation and transport at the surface of photocathodes. This has been achieved by Domen et al.[1−3] through surface modification of I−III−VI$_2$ photocathodes with *n*-type layers to form a *p-n* junction—facilitating a more efficient photogenerated charge separation. However, the mobility of charge carriers through the bulk of the photoelectrode is another important factor, which has received little attention to date. For charge carriers to contribute to PEC half-reactions, they must first reach the semiconductor/electrolyte or semiconductor/substrate interface; therefore, the internal electrical transport of the charge carriers is significant. In support of this statement, it is noted that several studies on hematite photoelectrodes for solar water splitting have taken a closer look at the poor bulk charge transport of this material to improve PEC water splitting.[4−6] Recently, van de Krol et al.[7] concluded that charge carrier transport is a major limiting factor in the photoconversion efficiency of *p*-$CuBi_2O_4$ for PEC water splitting. It was noted that the poor charge carrier transport of holes (the majority charge carrier) reduced the obtainable photocurrent density by 2 orders of magnitude. *n*-$BiVO_4$, a well-known and characterized metal oxide photoanode for PEC water splitting, is most limited in its photoresponse due to its poor bulk electronic conductivity.[8,9] The poor bulk electronic conductivity has been confirmed by time-resolved microwave conductivity studies and temperature dependent bulk transport studies.[10,11] It is clear from these studies on well-known PEC materials that the basic charge transport properties of other promising light-harvesting materials, like I−III−VI$_2$ chalcopyrites, merit deeper study in order to optimize them for further PEC applications.

The utilization of ternary chalcopyrite semiconductors for light-harvesting processes, such as PEC water splitting, stems from their innate, high optical absorption coefficients. Among I−III−VI$_2$ chalcopyrites, copper indium disulfide ($CuInS_2$) possesses a band gap that is well matched to the solar spectrum on Earth (1.5 eV). In addition to its spectral response, this material possesses favorable band edge energetics relative to H_2 evolution. Despite this favorable bandgap range and alignment, $CuInS_2$-based photocathodes have only been reported to achieve a maximum solar conversion efficiency of 1.82% (at +0.25 V vs RHE).[1] High bulk electrical resistivities have been reported as a contributing factor to the low efficiency of I−III−VI$_2$ materials when used as photocathodes,[12−14] as charge transport properties are one of the major factors (along with spectral response and band gap alignment) to consider for PEC processes.

The bulk, electrical properties of I−III−VI$_2$ materials largely depend on their atomic composition.[12,15−17] One method used to decrease resistivity in $CuInS_2$ is to introduce an aliovalent impurity atom into the system. This technique was employed on $CuInS_2$ thin films using an aliovalent Zn^{2+} impurity on the In^{3+} sites, which demonstrated a decrease in resistivity with an increase of Zn content up to 15%, generating the quaternary compound $CuIn_{0.85}Zn_{0.15}S_2$.[18] In other work, such as in the $CuGaS_2$−ZnS or $AgInS_2$−ZnS solid solutions, Zn is present, but the ZnS substitution is not nominally expected to yield a change in dopant concentration.[19,20] A related approach is to modify the ratio of cations in the structure; when varying the ratio of the cations in $CuInS_2$ thin films ($0.98 \leq Cu/In \leq 1.02$)

Received: April 3, 2017
Revised: July 24, 2017
Published: July 27, 2017

DOI: 10.1021/acs.jpcc.7b03152
J. Phys. Chem. C 2017, 121, 17046−17052

the resistivity can vary by 1 order of magnitude,[12,13] indium rich samples being the most resistive due to the compensation of the *p*-type defects present through the presence of donors.[21,22]

Studies reporting on the effect of anion ratio in $CuInS_2$ have introduced Se into the system, creating the series $CuIn(S_{1-x}Se_x)_2$ in nanoparticle or thin film form.[23−26] Although no transport studies on this series have been reported, these $CuInS_2$−$CuInSe_2$ alloys allow a linear tuning of the fundamental bandgap (E_g) from pure $CuInS_2$ (1.5 eV) to pure $CuInSe_2$ (1.0 eV). This E_g tuning could in turn increase efficiency of $CuInS_2$ systems for PEC applications by manipulating the position of the valence band edge of photocathodes.[25,26]

$CuIn(S_{1-x}Se_x)_2$ alloys not only offer the opportunity for E_g tuning, but also provide an environment for studying the effects of varying the bulk electrical resistivity on the efficiency of charge transport processes (like PEC H_2 evolution). High Se content reduces the absolute bandgap energy of the alloy away from optimal values and, additionally, shifts the absolute energy levels of the valence and conduction bands to potentials unsuitable for PEC applications.[27,28] However, limited substitution of Se for S can be expected to alleviate high resistivity issues in $CuInS_2$ while keeping the bandgap energy within range of the visible spectrum. The purpose of the current work is to elucidate the transport properties and bandgap trends of well characterized bulk materials in this series as a context for future PEC studies.

■ EXPERIMENTAL METHODS

Synthesis. Ternary and quaternary [we use the conventional term quaternary (four elements in major proportion) to describe the mixture of the two ternary compounds with different chalogenide end members] $CuIn(S_{1-x}Se_x)_2$ (x = 0, 0.2, 0.4, 0.6, 0.8, 1.0) polycrystalline ingots were prepared by loading stoichiometric amounts of elemental Cu (Sigma-Aldrich 99.999%), In (Alfa Aesar 99.99%), S (Alfa Aesar), and Se (Alfa Aesar 99.99%) into quartz ampules. Mg (Sigma-Aldrich 99.99%) was used as a *p*-type dopant on the In site for all transport property measurements. All samples were doped with 1% Mg, hereby abbreviated as Mg-$CuIn(S_{1-x}Se_x)_2$. Mg was chosen for the *p*-type dopant because of its high electropositive nature, ensuring efficient hole donation to the system. The ampules were purged with Ar and sealed under vacuum. The ampules were heated stepwise to 400, 700, and finally 1100 °C, annealing for 24 h at 400 and 700 °C to allow volatile S and Se vapor to react. After 6 h at 1100 °C, the samples were quenched to room temperature to allow maximum dopant dispersion in the crystal lattice. The resultant polycrystalline ingots were then ground into a powder and pressed into pellets (2.4 mm thickness, 3.17 cm^2 area) with 2 tons of pressure. The pellets were sintered under vacuum at 650 °C for 3 h. The resulting pellets (≥80% of theoretical density) were then used for subsequent characterization.

Sample Characterization. All structural characterization presented in this manuscript was performed on stoichiometric $CuIn(S_{1-x}Se_x)_2$. First-principles calculations on ternary chalcopyrites have revealed that divalent dopants like Mg are shallow acceptors on the group-III site.[29] Thus, the 1% Mg dopant needed for transport property measurements is not expected to change the characterization data beyond the measurement error of the analytical techniques employed. The polycrystalline ingots and sintered pellets were analyzed using powder X-ray diffraction (PXRD) on a Bruker D8 Advance Eco with Cu Kα radiation and a LynxEye-XE detector. The scan parameters were 0.02°/step with 0.085 s/step, for a total scan time of 8 min. A Quanta 200 field emission gun environmental scanning electron microscope (SEM) equipped with an integrated Oxford System was employed for energy dispersive X-ray (EDX) analysis. The X-ray penetration depth was 1−2 mm, and the detection limit of a specific element was 10%. X-ray photoelectron spectra (XPS) were collected under 10^{-9} Torr using a ThermoFisher K-Alpha X-ray photoelectron spectrometer. All spectra were recorded using Al Kα radiation (1487 eV) with a survey and pass energy of 100 and 20 eV, respectively. Measured peaks were fit using Casa XPS software and a Shirley background. The C 1s peak at 284.5 eV of adventitious hydrocarbon was used as an internal binding energy reference. Optical band-gaps were measured with a UV−vis diffuse reflectance HITACHI 131-9007-1 model U3210/U3410 recording spectrophotometer with incident light from 200 to 1300 nm. KBr was used as a calibration standard. Each sample pellet for absorbance measurement was made from a homogeneously ground mixture of the powder and KBr (1:20 by weight).

Transport Property Measurements. Transport property measurements were performed on the sintered polycrystalline pellet samples with 1% Mg dopant, Mg-$CuIn(S_{1-x}Se_x)_2$. Hall effect data and electrical resistivities were collected using a Quantum Design Physical Property Measurement System. The samples were cut from the pellets into 1.20 mm-thick rectangles, measuring approximately 1.5 mm × 0.5 mm in area. Hall effect data were obtained at 300 K by sweeping the magnetic field from −9 to +9 T at a constant current of 0.1 μA through the sample. The carrier concentration, N, was estimated by assuming a single dominant carrier type and the relationship

$$\frac{1}{Ne} = \frac{Rt}{B} \quad (1)$$

where e is the electron charge, R/B is the slope obtained from the measured Hall resistance vs magnetic field measurement, and t is the sample thickness. Resistivity (ρ) measurements were performed over a range of 395−10 K. Both Hall and resistivity four probe measurements were facilitated by attaching platinum wires to the samples using conductive Ag paint.

■ RESULTS AND DISCUSSION

Synthesis and Characterization of $CuIn(S_{1-x}Se_x)_2$. PXRD patterns of $CuIn(S_{1-x}Se_x)_2$ (x = 0, 0.2, 0.4 0.6, 0.8, 1.0) sintered pellets can be seen in Figure 1a. The variation of the S/Se ratio in the polycrystalline pellets is clearly reflected in the XRD data, without any evidence of a structural phase transition or phase separation throughout the series. The patterns show pure, tetragonal $CuInS_2$ chalcopyrite for x = 0, pure tetragonal $CuInSe_2$ chalcopyrite for x = 1.0, and homogeneous solid solutions for x = 0.2, 0.4, 0.6, and 0.8. As the Se content increases, the diffraction peaks shift toward lower 2θ angles, attributed to the increased lattice spacings when substituting Se atoms for smaller S atoms. $CuIn(S_{1-x}Se_x)_2$ lattice parameters a and c for the tetragonal crystal structures were determined from the refined XRD patterns and are listed in Table 1. The lattice parameters as a function of composition (x) are plotted in Figure 1b. The lattice parameters show a clear linear relationship with increasing Se content, consistent with Vegard's law behavior.

DOI: 10.1021/acs.jpcc.7b03152
J. Phys. Chem. C 2017, 121, 17046−17052

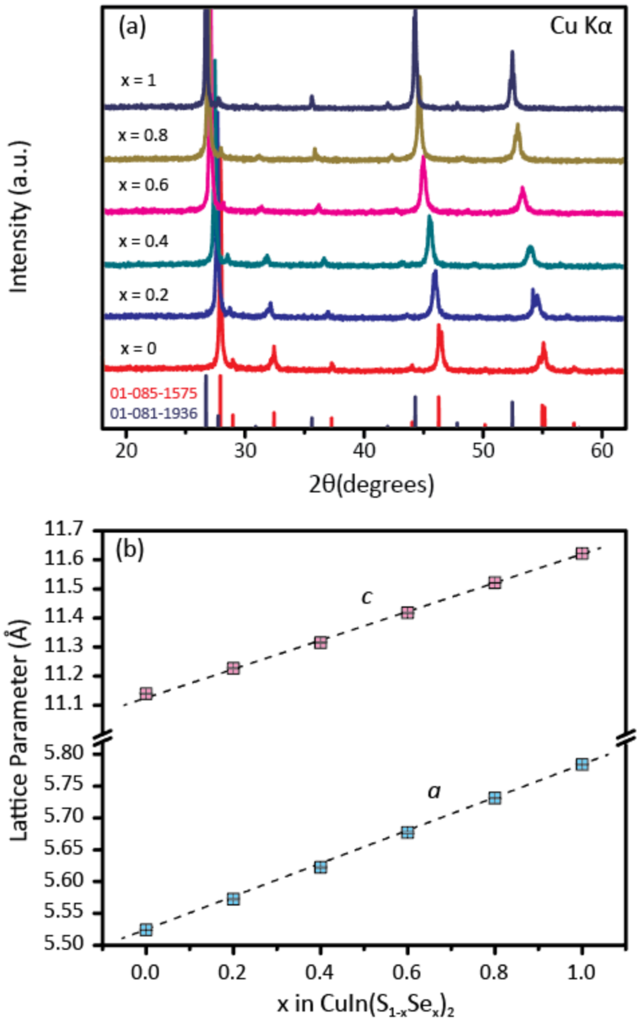

Figure 1. (a) PXRD patterns for the sintered pellets of $CuIn(S_{1-x}Se_x)_2$ for x = 0, 0.2, 0.4, 0.6, 0.8, and 1 recorded at 300 K. The red and purple lines on the bottom of the plot correspond to the powder pattern of tetragonal phase ($I\bar{4}2d$) for pure $CuInS_2$ and $CuInSe_2$, respectively. (b) Lattice parameters a and c plotted as a function of composition (x) displaying a clear linear increase in the unit cell as Se content increases. The dotted, linear trendline is a guide for the eyes.

Table 1. $CuIn(S_{1-x}Se_x)_2$ Material Characterization: Lattice Parameters a (Å) and c (Å); Mole Ratio of Cu, In, S, and Se as Measured by EDX; and E_g (eV) from UV-vis Diffuse Reflectance Measurements

x	a	c	Cu:In:S:Se	E_g
0.0	5.5240(6)	11.140(1)	1.00:1.02:1.98:0.0	1.39
0.2	5.572(1)	11.227(2)	1.17:1.02:1.69:0.4	1.24
0.4	5.622(2)	11.315(3)	1.18:1.02:1.13:0.8	1.16
0.6	5.677(1)	11.418(3)	1.01:1.08:0.8:1.12	1.09
0.8	5.7312(6)	11.521(1)	1.18:1.14:0.4:1.62	0.99
1.0	5.7838(5)	11.622(1)	1.08:1.00:0.0:1.92	0.92

The bulk chemical composition of the pellets was analyzed by EDX. The quantitative analysis (listed in Table 1) shows the smooth evolution of the material from pure $CuInS_2$ to pure $CuInSe_2$. Although the precision of the technique employed for a specific element is 10%, the Se content increases linearly with increasing x. This is shown in Figure 2a, where the Se content as detected by EDX is plotted as a function of Se content in the

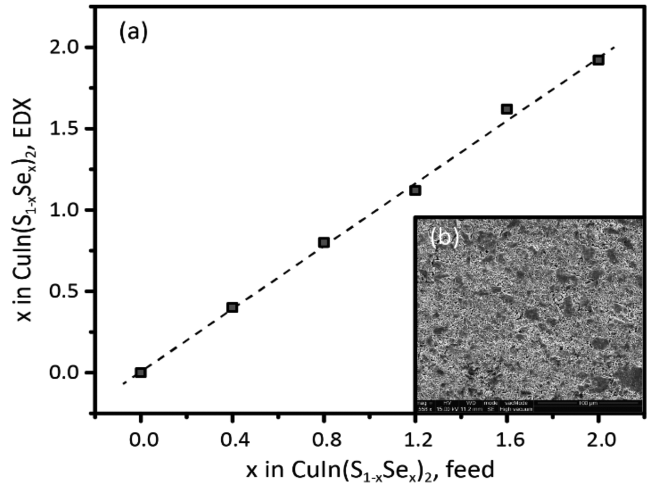

Figure 2. (a) Ratio of Se content in $CuIn(S_{1-x}Se_x)_2$ as measured by EDX as a function of Se content in the synthetic preparation feed. The dotted, linear trendline is a guide for the eyes. (b) Representative SEM image at 558× magnification for sample $CuIn(S_{1-x}Se_x)_2$ with x = 0.6, showing evenly distributed grain size of the dense, polycrystalline pellet.

synthetic feed.[30] A representative SEM image and corresponding EDX data of a dense $CuIn(S_{1-x}Se_x)_2$ pellet used in this study can be seen in Figure 2b. By SEM, the dense polycrystalline pellets display evenly distributed grain sizes along the entire pellet surface area. Several different points on each pellet were sampled. The 1% Mg dopant could not be quantified by EDX analysis due to characteristic X-ray overlap of Mg $K\alpha$ (1.253 keV) and Se $L\alpha$ (1.379 keV). XPS was used to probe the chemical composition on the surface of the pellets. All binding energies were referenced to C 1s (284.5 eV). Representative XPS spectra of $CuIn(S_{1-x}Se_x)_2$ where x = 0.6 can be seen in Figure 3. Figure 3a shows Cu 2p core splitting into Cu $2p_{3/2}$ (932.0 eV) and Cu $2p_{1/2}$ (951.8 eV) peaks with a

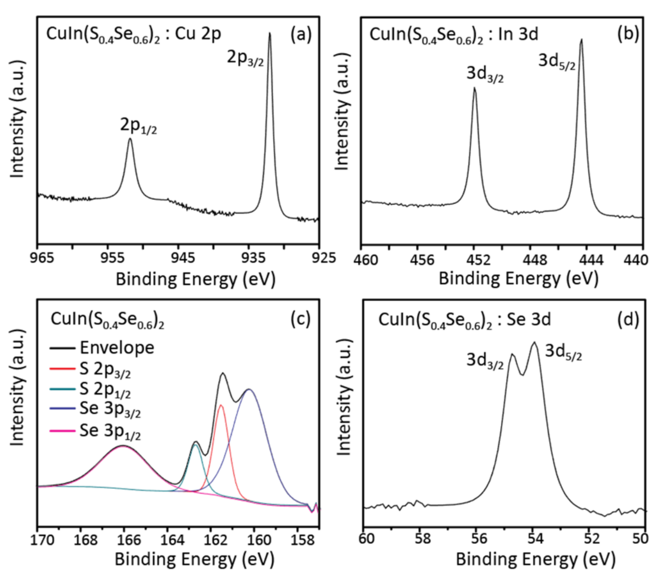

Figure 3. Representative XPS spectra of $CuIn(S_{1-x}Se_x)_2$ at x = 0.6. (a) Cu 2p peaks in the +1 oxidation state. (b) In 3d peaks in the +3 oxidation state. (c) Orbital deconvolution of the S 2p and Se 3p peak overlap. Both S and Se peaks are in the −2 oxidation state. (d) Se 3d peaks in the −2 oxidation state.

DOI: 10.1021/acs.jpcc.7b03152
J. Phys. Chem. C 2017, 121, 17046−17052

peak separation of 19.8 eV, signifying Cu is in the +1 oxidation state. Figure 3b shows the In 3d peaks located at 444.4 and 451.9 eV with a peak separation of 7.54 eV, signifying In is in the +3 oxidation state. Figure 3c shows the overlap region of S 2p and Se 3p. The S $2p_{3/2}$ is located at 161.5 eV and S $2p_{1/2}$ at 162.7 eV with a peak separation of 1.18 eV. The Se $3p_{3/2}$ is found at 160.2 eV and Se $3p_{1/2}$ (166.0 eV) with a peak separation of 5.8 eV. Both S 2p and Se 3p peak positions support a −2 oxidation state. Figure 3d shows the Se 3d region with Se $3d_{5/2}$ at 53.9 eV and Se $3d_{3/2}$ at 54.8 eV with a peak separation of 0.86 eV. The 1% Mg dopant could not be identified by XPS due to peak overlap with the Mg 2p (51 eV) and Se 3d (54 eV) signals.

Diffuse reflectance UV−vis was used to determine the optical bandgap of the opaque, dense pellets used in this study. Figure 4b shows the absorption spectra of the $CuIn(S_{1-x}Se_x)_2$ series.

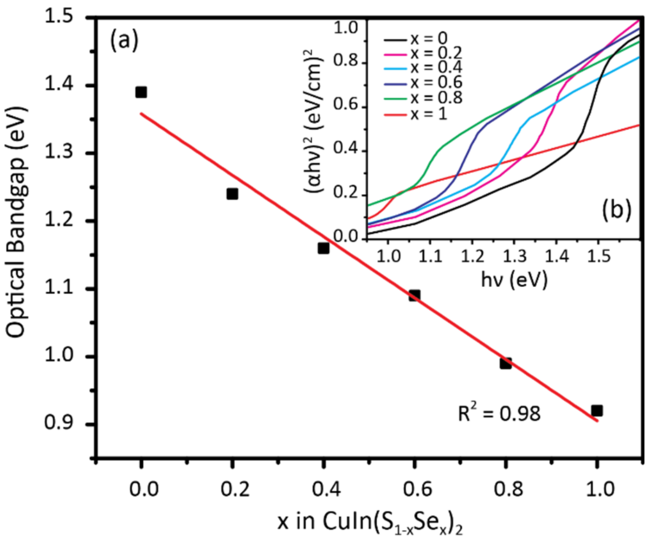

Figure 4. (a) Energy bandgap vs composition (x) of $CuIn(S_{1-x}Se_x)_2$ recorded at room temperature. (b) Diffuse reflectance UV−vis of $CuIn(S_{1-x}Se_x)_2$ series plotted as $(\alpha h\nu)^2$ (eV/cm)^2 versus $h\nu$ (eV). The optical bandgap energy, E_g, was estimated from extrapolating the linear absorption edge to the x axis.

The direct optical band gap (E_g) was established using a Tauc plot[31] considering the following relationship:

$$(\alpha h\nu)^2 = A/(h\nu - E_g) \quad (2)$$

where α is the absorption coefficient, A is a constant, and $h\nu$ is the radiation energy.[32] The experimental values of $(\alpha h\nu)^2$ were plotted against $h\nu$, and E_g was determined by extrapolating the absorption edge to the x intercept. These values are reported in Table 1. Figure 4a shows the linear decrease of the optical band gap E_g of $CuIn(S_{1-x}Se_x)_2$ from 1.39 to 0.92 eV with composition varying from x = 0 to 1. This linear relation agrees with previous optical bandgap studies on $CuIn(S_{1-x}Se_x)_2$ thin films[25,26] and, in addition, agrees with the prediction by Wu et al. in 2002 on the linear relationship of the band gap energy values of the mixed chalcopyrite $CuIn(S_xSe_{1-x})_2$ (x = 0.2, 0.4, 0.6, 0.8) solid solution with composition.[33]

Transport Properties of Mg-CuIn($S_{1-x}Se_x$)$_2$. The temperature-dependent bulk resistivity of each sample was probed on cooling from 395 K. A representative temperature profile of the electrical resistivity, for Mg-$CuIn(S_{1-x}Se_x)_2$ at x = 0.8, is plotted in Figure 5a from 300 to 150 K. All samples display an

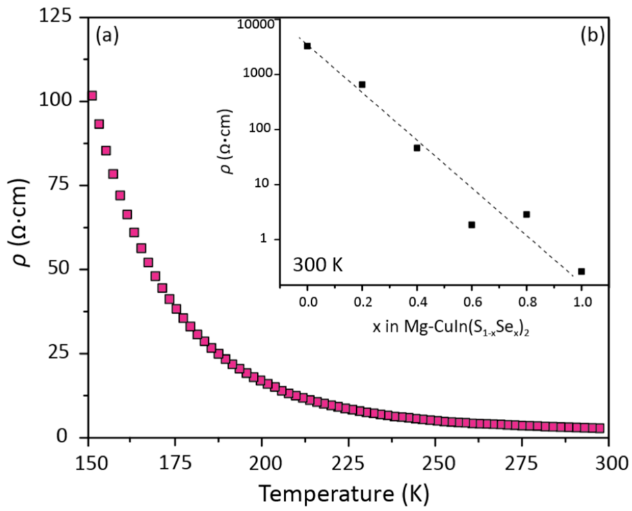

Figure 5. (a) Representative temperature profile of Mg-CuIn($S_{1-x}Se_x$)$_2$ for x = 0.8 ranging from 300 to 150 K. The same temperature profile is exhibited for all samples, with resistivity increasing as temperature decreases, a signature of semiconductor temperature profiles. (b) The ρ values at 300 K plotted with composition (x). A general decreasing trend is seen from x = 0 to 1, with a total decrease in ρ of 4 orders of magnitude. The dotted, linear trendline is a guide for the eyes.

exponentially increasing resistivity with decreasing temperature, a signature of semiconducting materials. The bulk resistivity of each sample at 300 K is listed in Table 2. To highlight the

Table 2. Carrier Transport Properties for Mg-CuIn($S_{1-x}Se_x$)$_2$

x	resistivity (Ω cm)	p-type carrier concentration (cm^{-3})	mobility (cm^2 V^{-1} s^{-1})	E_a (meV)
0.0	3300	1.6×10^{15}	1.2	70
0.2	650	8.7×10^{15}	1.1	49
0.4	46	1.2×10^{17}	1.2	35
0.6	1.9	5.2×10^{17}	6.1	33
0.8	2.9	1.3×10^{18}	1.6	25
1.0	0.26	2.7×10^{18}	8.9	7.2

general decreasing trend in resistivity from x = 0 to 1, the resistivity (ρ) vs composition (x) at 300 K is plotted in Figure 5b. The plot shows that the transition from x = 0 to 1 does not have perfect linear behavior. This nonlinear behavior can be attributed to the interplay of both intrinsic defects and the Mg dopant in the crystal lattice.[34] To elucidate the charge transport energetics present in the temperature range near room temperature (395−250 K), the resistivity data for all samples is plotted as log(ρ) vs T^{-1} in Figure 6b. The activation energy was thus estimated for each sample based on the relationship:

$$\rho = \rho_0 \exp\left(\frac{-E_a}{k_B T}\right) \quad (3)$$

where ρ is the sample resistivity, ρ_0 is the pre-exponential term, k_B is Boltzmann's constant, and T is the temperature. When plotting log(p) vs T^{-1}, as in Figure 6, a linear semilogarithmic fit can be made to estimate E_a values. The calculated E_a's are much less than half of the optical band gaps measured by UV−vis diffuse reflectance spectrophotometry (Table 1), indicating that all materials are in the extrinsic semiconductor regime near

DOI: 10.1021/acs.jpcc.7b03152
J. Phys. Chem. C 2017, 121, 17046−17052

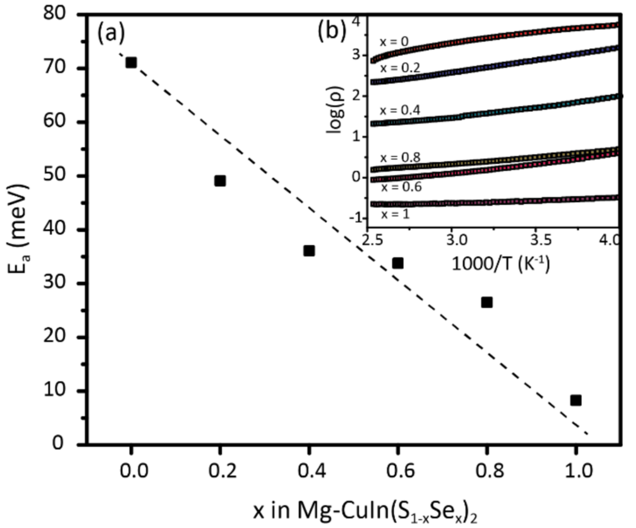

Figure 6. (a) Activation energy (E_g) vs x for all of the composition series. As Se content increases, it is kinetically easier for transport of holes through the valence band. The dotted, linear trendline is a guide for the eyes. (b) The log(ρ) vs 1000/T in the temperature range of 395−250 K, in order to extract the E_a for each sample.

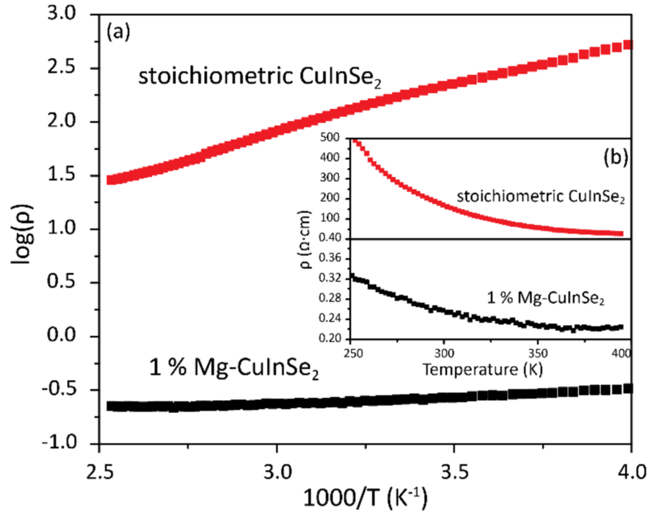

Figure 7. (a) log(ρ) vs 1000/T for the temperature range of 395−250 K comparing stoichiometric $CuInSe_2$ to the 1% Mg-doped $CuInSe_2$. The difference in the slopes in clear, with stoichiometric $CuInSe_2$ displaying a much steeper slope, signifying stoichiometric $CuInSe_2$ has a larger activation energy than 1% Mg-doped $CuInSe_2$. (b) Inset shows the ρ vs T profile for both stoichiometric $CuInSe_2$ and 1% Mg doped $CuInSe_2$ in the same temperature range.

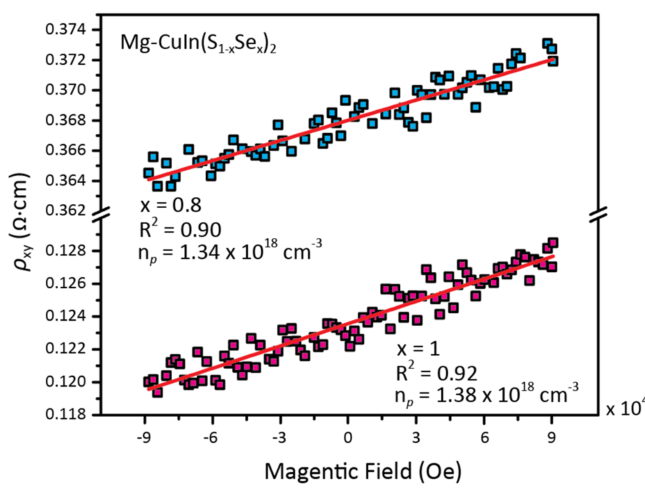

Figure 8. Representative Hall measurements for Mg-CuIn$(S_{1-x}Se_x)_2$ for x = 0.8 and 1 measured for the magnetic field from −9 to +9 T. The positive slopes from this plot were extracted to calculate the p-type carrier concentrations. The red solid lines are the linear fit to the experimental data points.

room temperature, with acceptor level defects dominating the transport. Thus, the E_a values represent the estimated acceptor ionization energies for each sample and are reported in Table 2. Figure 6a shows the E_a values reported in Table 2 as a function of composition (x). A general decreasing trend is seen going from x = 0 to 1. This suggests that as the Se content increases the acceptor energies become more shallow.

To clarify the identity of the extrinsic acceptor defect as our Mg dopant and indirectly validate the presence of Mg in our samples, a stoichiometric sample of $CuInSe_2$ was analyzed. The resistivity was probed in the same temperature range, and the resulting data was used to calculate its activation energy. Figure 7a shows the log(ρ) vs T^{-1} plot (Figure 7b shows the resistivity temperature profile) comparing the resistivities of stoichiometric $CuInSe_2$ and 1% Mg-doped $CuInSe_2$. It is clear from Figure 7a that the slope of the stoichiometric sample is much steeper, signifying a higher activation energy. In the temperature regime near room temperature (395−250 K), the E_a for stoichiometric $CuInSe_2 \approx$ 83 meV, over ten times the activation barrier found in the Mg-doped sample. We attribute the acceptor level defect to the presence of Mg dopant, showing the Mg dopant does indeed have acceptor levels lying below the Fermi level of all semiconductor samples. Similar measurements on stoichiometric $CuInS_2$ were attempted, but nondoped samples of this material had a resistivity above the measurement limit of our apparatus, supporting the presence of Mg dopant in our samples.

Majority carrier concentrations were estimated by Hall measurements. Representative Hall resistivity data as a function of magnetic field for Mg-CuIn$(S_{1-x}Se_x)_2$, x = 1 and 0.8 with 1% Mg dopant at 300 K are shown in Figure 8. The samples exhibit a reliable linear fit of the Hall data ($R^2 \geq 0.90$) to applied field, allowing for the majority carrier concentrations (n_p) to be estimated (Table 2). For samples x = 0.8 and 1, n_p ($\sim 10^{18}$ cm^{-3}) is 3 orders of magnitude greater than for samples x = 0 and 0.2 ($\sim 10^{15}$ cm^{-3}). Despite all samples being synthesized with the same amount of p-type dopant (1% Mg) this increase in n_p at high values of x is expected given the innate difference in acceptor level depths and band gap energies between pure $CuInS_2$ and $CuInSe_2$. Samples x = 0.4 and 0.6 display carrier concentrations of $\sim 10^{17}$ cm^{-3}.

Once the carrier concentrations were in hand, the mobilities of the majority carriers were estimated by assuming a single dominant carrier and band-like carrier motion. Using the measured quantities and the relationship

$$\sigma = Ne\mu \tag{4}$$

where σ is the conductivity at 300 K, μ is the mobility of the carrier, e is the the electron charge, and N is the carrier concentration, the mobilities were estimated (Table 2) as varying from approximately 1−10 cm^2 V^{-1} s^{-1}. The 4-order-of-magnitude decrease in bulk electrical resistivity seen as x increases from 0 to 1 can therefore be primarily attributed to an

DOI: 10.1021/acs.jpcc.7b03152
J. Phys. Chem. C 2017, 121, 17046−17052

increase in carrier concentration but also to a much smaller increase in mobility.

CONCLUSIONS

Temperature-dependent bulk resistivity and Hall effect measurements revealed a 4-order-of-magnitude decrease in electrical resistivity with increasing x value in the quaternary alloy system $CuIn(S_{1-x}Se_x)_2$. Hall measurements revealed a corresponding 3-order-of-magnitude increase in p-type carrier concentration with increasing the x value. The extrapolated electrical mobilities of the p-type majority carriers of $CuIn(S_{1-x}Se_x)_2$ were determined to increase somewhat with x. The use of 1% Mg-dopant in $CuIn(S_{1-x}Se_x)_2$ enabled the study of the bulk resistivity of the materials near ambient temperature. The bandgap and carrier transport properties presented here strongly suggest that the chalcopyrite series $CuIn(S_{1-x}Se_x)_2$ warrants further study as photoelectrodes to fully realize their potential for PEC applications.

AUTHOR INFORMATION

Corresponding Authors

*E-mail: rcava@princeton.edu.
*E-mail: bocarsly@princeton.edu.

ORCID

Andrew B. Bocarsly: 0000-0003-3718-0933

Notes

The authors declare no competing financial interest.

ACKNOWLEDGMENTS

This material is based upon work supported by the National Science Foundation Graduate Research Fellowship under Grant No. 1656466. We gratefully acknowledge the U.S. Department of Energy for financial support: A.B.B. would like to acknowledge Grant DE-AC02-05CH11231 and R.J.C. would like to acknowledge Grant DE-F602-98ER45706. We thank John Schreiber and Nan Yao for invaluable assistance with X-ray photoelectron spectroscopy and scanning electron microscopy. The manuscript was written through contributions of all authors.

REFERENCES

(1) Zhao, J.; Minegishi, T.; Zhang, L.; Zhong, M.; Gunawan, N.; Nakabayashi, M.; Ma, G.; Hisatoni, T.; Katayama, M.; Ikeda, S.; et al. Enhancement of Solar Hydrogen Evolution from Water by Surface Modification with CdS and TiO_2 on Porous $CuInS_2$ Photocathodes Prepared by an Electrodeposition-Sulfurization Method. *Angew. Chem., Int. Ed.* **2014**, *53*, 11808−11812.
(2) Moriya, M.; Minegishi, T.; Kumagai, H.; Katayama, M.; Kubota, J.; Domen, K. Stable Hydrogen Evolution from CdS-Modified $CuGaSe_2$ Photoelectrode under Visible-Light Irradiation. *J. Am. Chem. Soc.* **2013**, *135*, 3733−3735.
(3) Zhang, L.; Minegishi, T.; Nakabayashi, M.; Suzuki, Y.; Seki, K.; Shibata, N.; Kubota, J.; Domen, K. Durable Hydrogen Evolution from Water Driven by Sunlight Using $(Ag,Cu)GaSe_2$ Photocathodes Modified with CdS and $CuGa_3Se_5$. *Chem. Sci.* **2015**, *6*, 894−901.
(4) Shen, S.; Kronawitter, C. X.; Jiang, J.; Guo, L.; Mao, S. S. Surface Modification of α-Fe_2O_3 Nanorod Array Photoanodes for Improved Light-Induced Water Splitting. *MRS Online Proc. Libr.* **2011**, *1326*, 10.1557/opl.2011.1045.
(5) Shen, S. Toward Efficient Solar Water Splitting over Hematite Photoelectrodes. *J. Mater. Res.* **2014**, *29*, 29−46.
(6) Yuan, Y.; Gu, J.; Ye, K. H.; Chai, Z.; Yu, X.; Chen, X.; Zhao, C.; Zhang, Y.; Mai, W. Combining Bulk/Surface Engineering of Hematite to Synergistically Improve Its Photoelectrochemical Water Splitting Performance. *ACS Appl. Mater. Interfaces* **2016**, *8*, 16071−16077.
(7) Berglund, S. P.; Abdi, F. F.; Bogdanoff, P.; Chemseddine, A.; Friedrich, D.; van de Krol, R. Comprehensive Evaluation of $CuBi_2O_4$ as a Photocathode Material for Photoelectrochemical Water Splitting. *Chem. Mater.* **2016**, *28*, 4231−4242.
(8) Zhang, K.; Shi, X. J.; Kim, J. K.; Park, J. H. Photoelectrochemical Cells with Tungsten Trioxide/Mo-Doped $BiVO_4$ Bilayers. *Phys. Chem. Chem. Phys.* **2012**, *14*, 11119−11124.
(9) Abdi, F. F.; van de Krol, R. Nature and Light Dependence of Bulk Recombination in Co-Pi-Catalyzed $BiVO_4$ photoanodes. *J. Phys. Chem. C* **2012**, *116*, 9398−9404.
(10) Abdi, F. F.; Savenije, T. J.; May, M. M.; Dam, B.; van de Krol, R. The Origin of Slow Carrier Transport in $BiVO_4$ thin Film Photoanodes: A Time-Resolved Microwave Conductivity Study. *J. Phys. Chem. Lett.* **2013**, *4*, 2752−2757.
(11) Rettie, A. J.; Lee, H. C.; Marshall, L. G.; Lin, J. F.; Capan, C.; Lindemuth, J.; McCloy, J. S.; Zhou, J.; Bard, A. J.; Mullins, C. B. Combined Charge Carrier Transport and Photoelectrochemical Characterization of $BiVO_4$ Single Crystals: Intrinsic Behavior of a Complex Metal Oxide. *J. Am. Chem. Soc.* **2013**, *135*, 11389−96.
(12) Sebastian, T.; Jayakrishnan, R.; Kartha, C. S.; Vijayakumar, K. P. Characterization of Spray Pyrolysed $CuInS_2$ Thin Films. *Open Surf. Sci. J.* **2009**, *1*, 1−6.
(13) Mere, A.; Kijatkina, O.; Rebane, H.; Krustok, J.; Krunks, M. Electrical Properties of Sprayed $CuInS_2$ Films for Solar Cells. *J. Phys. Chem. Solids* **2003**, *64*, 2025−2029.
(14) Cherian, A. S.; Abe, T.; Kashiwaba, Y.; Kartha, C. S.; Vijayakumar, K. P. $CuInS_2/In_2S_3$ Cells Using a Cost-Effective Technique: Significance of Precursor Ratios on Cell Parameters. *Energy Procedia* **2012**, *15*, 283−290.
(15) John, T. T.; Wilson, K. C.; Kumar, P. M. R.; Kartha, C. S.; Vijayakumar, K. P.; Kashiwaba, Y.; Abe, T.; Yasuhiro, Y. $CuInS_2$ Films Using Repeated Chemical Spray Pyrolysis. *Phys. Status Solidi A* **2005**, *1*, 79−84.
(16) Yukawa, T.; Kuwabara, K.; Koumoto, K. Electrodeposition of $CuInS_2$ from Aqueous Solution (II) Electrodeposifion of $CuInS_2$ Film. *Thin Solid Films* **1996**, *286*, 151−153.
(17) Bandyopadhyaya, S.; Chaudhuri, S.; Pal, A. K. Synthesis of $CuInS_2$ Films by Sulphurization of Cu/In Stacked Elemental Layers. *Sol. Energy Mater. Sol. Cells* **2000**, *60*, 323−339.
(18) Ben Rabeh, M.; Chaglabou, N.; Kanzari, M.; Rezig, B. Structural and Optical Studies on Antimony and Zinc Doped $CuInS_2$ Thin Films. *Phys. Procedia* **2009**, *2*, 745−750.
(19) Kato, T.; Hakari, Y.; Ikeda, S.; Jia, Q.; Iwase, A.; Kudo, A. Utilization of Metal Sulfide Material of $(CuGa)_{1-x}Zn_{2x}S_2$ Solid Solution with Visible Light Response in Photocatalytic and Photoelectrochemical Solar Water Splitting Systems. *J. Phys. Chem. Lett.* **2015**, *6*, 1042−1047.
(20) Tang, X.; Ho, W. B. A.; Xue, J. M. Synthesis of Zn-Doped $AgInS_2$ Nanocrystals and Their Fluorescence Properties. *J. Phys. Chem. C* **2012**, *116*, 9769−9773.
(21) Tiwari, A. N.; Pandya, D. K.; Chopra, K. L. Electrical and Optical Properties of Single-Phase Cuins2 Films Prepared Using Spray Pyrolysis. *Thin Solid Films* **1985**, *130*, 217−230.
(22) Sebastian, T.; Gopinath, M.; Sudha Kartha, C.; Vijayakumar, K. P.; Abe, T.; Kashiwaba, Y. Role of Substrate Temperature in Controlling Properties of Sprayed $CuInS_2$ Absorbers. *Sol. Energy* **2009**, *83*, 1683−1688.
(23) Neff, H.; Lange, P.; Fearheiley, M. L.; Bachmann, K. J. Optical and Electrochemical Properties of $CuInSe_2$ and $CuInS_2$-$CuInSe_2$ Alloys. *Appl. Phys. Lett.* **1985**, *47*, 1089.
(24) Chiang, M.-Y.; Chang, S.-H.; Chen, C.-Y.; Yuan, F.-W.; Tuan, H.-Y. Quaternary $CuIn(S_{1-x}Se_x)_2$ Nanocrystals: Facile Heating-up Synthesis, Band Gap Tuning, and Gram-Scale Production. *J. Phys. Chem. C* **2011**, *115*, 1592−1599.
(25) Chavhan, S.; Sharma, R. Growth, Structural and Optical Properties of Non-Stoichiometric $CuIn(S_{1-x}Se_x)_2$ Thin Films

Deposited by Solution Growth Technique for Photovoltaic Application. *J. Phys. Chem. Solids* **2006**, *67*, 767−773.
(26) Subbaramaiah, K.; Raja, V. S. Structural and Optical Properties of Spray-Deposited $CuIn(S_{1-x}Se_x)_2$ Thin Films. *Thin Solid Films* **1992**, *208*, 247−251.
(27) Jaffe, J. E.; Zunger, A. Electronic Structure of the Ternary Chalcopyrite Semiconductors $CuAlS_2$, $CuGaS_2$, $CuInS_2$, $CuAlSe_2$, $CuGaSe_2$, and $CuInSe_2$. *Phys. Rev. B: Condens. Matter Mater. Phys.* **1983**, *28*, 5822−5847.
(28) Schmid, D.; Ruckh, M.; Grunwald, F.; Schock, H. W. Chalcopyrite/Defect Chalcopyrite Heterojunctions on the Basis of $CuInSe_2$. *J. Appl. Phys.* **1993**, *73*, 2902−2909.
(29) Persson, C.; Zhao, Y.-J.; Lany, S.; Zunger, A. N-Type Doping of $CuInSe_2$ and $CuGaSe_2$. *Phys. Rev. B: Condens. Matter Mater. Phys.* **2005**, *72*, 10.1103/PhysRevB.72.035211.
(30) Landry, C. C.; Lockwood, J. A.; Barron, A. R. Synthesis of Chalcopyrite Semiconductors and Their Solid Solutions by Microwave Irradiation. *Chem. Mater.* **1995**, *7*, 699−706.
(31) Tauc, J.; Grigorovici, R.; Vancu, A. Optical Properties and Electronic Structure of Amorphous Germanium. *Phys. Status Solidi B* **1966**, *15*, 627−637.
(32) Laidoudi, S.; Bioud, A. Y.; Azizi, A.; Schmerber, G.; Bartringer, J.; Barre, S.; Dinia, A. Growth and Characterization of Electrodeposited Cu_2O Thin Films. *Semicond. Sci. Technol.* **2013**, *28*, 115005.
(33) Zeng, Y.; Chua, S. J.; Wu, P. On the Prediction of Ternary Semiconductor Properties by Artificial Intelligence Methods. *Chem. Mater.* **2002**, *14*, 2989−2998.
(34) Myers, H. P. *Introductory Solid State Physics*, 2ed ed.; Taylor & Francis: London, 1997; Vol. *2*, p 536.

DOI: 10.1021/acs.jpcc.7b03152
J. Phys. Chem. C 2017, 121, 17046−17052